



# Manchester Metropolitan University

---

Kreider, Melissa E and Gallo, Alessandro and Back, Seoin and Liu, Yunzhi and Siahrostami, Samira and Nordlund, Dennis and Sinclair, Robert and Nørskov, Jens K and King, Laurie A and Jaramillo, Thomas F (2019) Precious Metal-Free Nickel Nitride Catalyst for the Oxygen Reduction Reaction. *ACS Applied Materials and Interfaces*, 11 (30). pp. 26863-26871. ISSN 1944-8244

---

**Downloaded from:** <http://e-space.mmu.ac.uk/624296/>

**Version:** Accepted Version

**Publisher:** American Chemical Society (ACS)

**DOI:** <https://doi.org/10.1021/acsami.9b07116>

Please cite the published version

<https://e-space.mmu.ac.uk>

# 1 Precious Metal-Free Nickel Nitride Catalyst for the Oxygen 2 Reduction Reaction

3 Authors: Melissa E. Kreider<sup>1</sup>, Alessandro Gallo<sup>1,2</sup>, Seoin Back<sup>1,3</sup>, Yunzhi Liu<sup>4</sup>, Samira  
4 Siahrostami<sup>1,6</sup>, Dennis Nordlund<sup>5</sup>, Robert Sinclair<sup>4</sup>, Jens K. Nørskov,<sup>1,2,7</sup> Laurie A. King<sup>1</sup>,  
5 Thomas F. Jaramillo<sup>1,2</sup>

## 6 Affiliations:

7 <sup>1</sup> Department of Chemical Engineering, Stanford University, 443 Via Ortega, Stanford, California  
8 94305, United States

9 <sup>2</sup> SUNCAT Center for Interface Science and Catalysis, SLAC National Accelerator Laboratory,  
10 2575 Sand Hill Road, Menlo Park, California 94025, United States

11 <sup>3</sup> Department of Chemical Engineering, Carnegie Mellon University, Pittsburgh, Pennsylvania  
12 15213, United States

13 <sup>4</sup> Department of Materials Science and Engineering, Stanford University, 496 Lomita Mall,  
14 Stanford, California 94305, United States

15 <sup>5</sup> Stanford Synchrotron Radiation Lightsource, SLAC National Accelerator Laboratory, 2575 Sand  
16 Hill Road, Menlo Park, California 94025, United States

17 <sup>6</sup> Department of Chemistry, University of Calgary, 2500 University Drive NW, Calgary, Alberta,  
18 Canada T2N 1N4

19 <sup>7</sup> Technical University of Denmark, DK-2800 Lyngby, Denmark  
20

## 21 Corresponding authors:

22 Laurie A. King email: lking10@stanford.edu

23 Thomas F. Jaramillo email: jaramillo@stanford.edu

## 24 Abstract:

25 With promising activity and stability for the oxygen reduction reaction (ORR), transition  
26 metal (TM) nitrides are an interesting class of non-platinum group catalysts for polymer  
27 electrolyte membrane fuel cells (PEMFCs). Here we report an active thin film nickel nitride  
28 catalyst synthesized through a reactive sputtering method. In RDE testing in 0.1M HClO<sub>4</sub>  
29 electrolyte, the crystalline nickel nitride film achieved high ORR activity and selectivity to  
30 4 electron ORR. It also exhibited good stability during 10 h and 40 h chronoamperometry  
31 (CA) measurements in acid and alkaline, respectively. A combined experiment-theory  
32 approach, with detailed *ex-situ* characterization with TEM and NEXAFS to reveal a mixed  
33 Ni<sub>4</sub>N/Ni<sub>3</sub>N structure with an amorphous surface oxide and DFT calculations to provide  
34 insight into the surface structure during catalysis, is highlighted. Design strategies for  
35 activity and stability improvement through alloying and nanostructuring are discussed.

36

## 37 Keywords:

38 Electrocatalysis, oxygen reduction reaction, non-precious metal catalysts, transition metal  
39 nitrides, reactive sputter deposition, density functional theory

1  
2  
3  
4  
5  
6  
7  
8  
9  
10  
11  
12  
13  
14  
15  
16  
17  
18  
19  
20  
21  
22  
23  
24  
25  
26  
27  
28  
29  
30  
31  
32  
33  
34  
35  
36  
37  
38

### **Introduction**

Proton-exchange membrane fuel cells (PEMFCs) are a promising technology towards enabling efficient and clean electricity production for transportation and industrial applications. In a PEMFC, hydrogen fuel is oxidized at the anode and oxygen is reduced at the cathode, generating electricity and releasing water as a benign by-product. Current commercial PEMFCs utilize expensive platinum-based catalysts for both the anode and cathode.<sup>1</sup> In particular, prohibitively large Pt loadings are required at the cathode to overcome the sluggish kinetics of the oxygen reduction reaction (ORR).<sup>2,3</sup> While much work has focused on improving the mass activity of Pt ORR catalysts,<sup>4-7</sup> limitations, including scarcity, instability, and susceptibility to carbon monoxide poisoning, remain.<sup>8-10</sup> Therefore, the discovery of earth abundant, non-precious metal ORR catalysts is of critical interest for the large scale implementation of fuel cell technology.

Many non-platinum group (non-PGM) materials have been explored for ORR, including transition metal oxide<sup>11,12</sup> and nitrogen-doped carbon<sup>13</sup> catalysts that have shown promising activity in alkaline electrolyte, and metal-nitrogen-carbon<sup>14-16</sup> catalysts that have achieved Pt-like activity in acid. Another promising class of earth-abundant materials are the transition metal nitrides, which are electronically conductive and have shown enhanced catalytic activity relative to their parent metal due to beneficial changes in the d-band structure.<sup>17</sup> Moreover, nitrides have achieved activity approaching that of the noble metals for a variety of reactions.<sup>18</sup> ORR activity has been demonstrated for several nitrides, including Co, Fe, and Ti.<sup>19-24</sup> Nitrides of Mo and W have also shown promising stability in acidic electrolyte due to their high corrosion resistance.<sup>25-27</sup> Particular interest has focused on the bimetallic nitride  $\text{Co}_{0.6}\text{Mo}_{1.4}\text{N}_2$ , which combines the activity of  $\text{Co}_x\text{N}$  with the acid stability of  $\text{Mo}_x\text{N}$ .<sup>28-30</sup>

Nickel-based nitride catalysts have also shown some ORR activity. Specifically, a high surface area  $\text{Ni}_3\text{N}$  on Ni-foam catalyst demonstrated low overpotential and good stability for HER and OER, as well as preliminary evidence of activity for ORR in alkaline media.<sup>31</sup>  $\text{Ni}_3\text{FeN}$  nanostructures have shown promising bifunctional activity, both as supports and catalysts, for metal-air batteries in alkaline media.<sup>32-34</sup> Additionally,  $\text{Ni}_3\text{N}$  quantum dots supported on NiO nanosheets have shown good activity and stability for ORR in alkaline.<sup>35</sup> Herein, we demonstrate an ORR active nickel nitride catalyst in acid for the first time. Through extensive electrochemical, materials, and theoretical characterization of a well-defined, carbon-free thin film catalyst, we investigate the fundamental ORR activity, selectivity, and stability of nickel nitride in both acidic and alkaline electrolyte. DFT is utilized to construct Pourbaix diagrams and identify the active surface of the catalyst.

1

## 2 **Materials and Methods**

### 3 **Materials**

4 Glassy carbon electrodes (Pine Research Instrument, 0.196 cm<sup>2</sup> geometrical area),  
5 graphite counter electrode, platinum wire, silicon wafers (WRS, 100 mm, P/Bor <100>,  
6 10-20 Ohm-cm), Ni sputtering target (Kurt J Lesker, 99.99% purity, 2" diameter), Ti  
7 sputtering target (Kurt J Lesker, 99.99% purity, 2" diameter), perchloric acid (Honeywell  
8 Fluka, 70%), potassium hydroxide (Fisher Chemical, 86.4% assay), were all used as  
9 received and without further purification unless otherwise stated.

10

### 11 **Synthesis**

12 Nickel nitride thin films were prepared by DC reactive sputtering using a Lesker Sputter.  
13 Prior to the nitride synthesis, a 20 nm thick Ti sticking layer was synthesized by sputter  
14 deposition (3 minutes, 200W, 100% Ar, 3 mTorr) onto the polished glassy carbon disk  
15 electrode. Subsequently, without breaking vacuum, the Ni target was sputtered in a  
16 mixture of 75% Ar, 25% N<sub>2</sub> plasma to deposit ~130 nm of Ni<sub>x</sub>N. The magnetron power  
17 supply was maintained at 200 W and the chamber pressure was 8 mTorr. The substrate  
18 was held at 180 ± 10 °C with a substrate bias of 100 V throughout the deposition. The  
19 Ni<sub>3</sub>N and Ni<sub>4</sub>N standards used for near edge X-ray absorption fine structure (NEXAFS)  
20 spectroscopy were synthesized on silicon substrates; Ni<sub>3</sub>N was made by increasing  
21 chamber pressure to 18 mTorr, while Ni<sub>4</sub>N was made by decreasing the substrate  
22 temperature to 90 °C. Ni and NiO thin films were synthesized using the same conditions,  
23 but with 100% Ar and 20% O<sub>2</sub> & 80% Ar plasma, respectively. Films were also  
24 synthesized on Si wafers, with native SiO<sub>2</sub> layer, for structural characterization.

### 25 **Physical characterization**

26 Grazing-incidence X-ray diffraction (XRD) data were obtained using a D8 Venture single  
27 crystal diffractometer (Bruker, λ=1.5418 Å) at an incidence angle of 5°. Top-down and  
28 cross-sectional scanning electron microscopy (SEM) was conducted with a FEI Magellan  
29 400 XHR SEM. X-ray photoelectron spectroscopy (XPS) was performed with a Phi  
30 Versaprobe 1 using monochromatized Al Kα (1486 eV) radiation. All XPS spectra were  
31 calibrated to the C 1s peak at a binding energy of 284.8 eV. CasaXPS software was used  
32 to perform peak fitting with Shirley backgrounds.

33 The cross-section TEM specimen was prepared conventionally.<sup>36</sup> The samples were  
34 glued and mechanically grounded to approximately 15 μm in thickness. The cross-section  
35 specimen was further ion milled until electron transparent in a Gatan PIPS II ion milling  
36 machine. Argon ion beams with 5 keV energy were induced at an incident angle of 5  
37 degrees to create a hole at the center of the specimen. After the formation of the hole,

1 the beam energy was gradually reduced to 0.5 keV for final cleaning. TEM experiments  
2 were conducted in a FEI Titan 80-300 environmental transmission electron microscope  
3 equipped with a spherical aberration corrector in the image-forming (objective) lens.  
4 Selected Area Diffraction Patterns (SADP) were calibrated using a standard Si [110]  
5 diffraction pattern taken under the same conditions.

6 NEXAFS data for N and O K-edge and Ni L-edge were collected at the Stanford  
7 Synchrotron Radiation Light Source (SSRL) on BL 8-2 and 10-1 in total fluorescence yield  
8 (TFY) and total electron yield (TEY) modes, operating the monochromator with 0.2 eV  
9 (for N and O K-edges) and 0.3 eV (for Ni L-edge) resolution, respectively. NiO, Ni<sub>3</sub>N, and  
10 Ni<sub>4</sub>N were used as standards. The collected data were normalized to the edge jump after  
11 subtraction of the pre-edge region. TFY enables bulk sensitivity with a penetration depth  
12 on the order of 100 nm, while TEY has a penetration depth of 5-10 nm.

13 NEXAFS simulations for the N K-edge were conducted with OCEAN code<sup>37,38</sup> and FEFF  
14 9 code<sup>39</sup> using a broadening of 1.0 eV and 0.52 eV, respectively, and the crystallographic  
15 structures of Ni<sub>4</sub>N and Ni<sub>3</sub>N. O K-edge was simulated with the FEFF 9 code using a SCF  
16 cluster of 6 Å and increasing the radius of the FMS cluster from 3 Å to 9 Å starting from  
17 the crystallographic structure of NiO. A broadening of 0.8 eV was applied to simulate the  
18 experimental broadening (primarily instrumental, core-hole, and vibrational broadening).  
19 The screening of the core-hole was computed using random phase approximation (RPA)  
20 and the H-L self-energy was used for the calculation of the exchange correlation potential.

## 21 **Electrochemical Testing**

22 Electrochemistry was performed using a rotating disk electrode (Pine Research  
23 Instrument) in a three-electrode glass cell, with 0.1 M HClO<sub>4</sub> or 0.1 M KOH electrolyte  
24 purged with oxygen or nitrogen. An in-house built reversible hydrogen electrode (RHE)  
25 was used as the reference electrode and a graphite rod as the counter electrode. The  
26 series resistance of the cell was measured at 100 kHz and the iR losses were  
27 compensated at 85%. The remaining 15% was corrected after testing. Electrochemical  
28 activity was assessed using cyclic voltammetry (CV), sweeping reversibly from 0.8 V to  
29 0.05 V at a scan rate of 20 mV/s using a Biologic VSP-300 Potentiostat. Unless otherwise  
30 stated, the oxygen purged voltammograms were corrected for background current by  
31 subtracting the baseline (nitrogen) sweep. For simplicity, only cathodic CV sweeps are  
32 shown in the main text; full CVs are shown in the SI. Stability was evaluated using  
33 chronoamperometry, holding at a constant potential of 0.15 V. Selectivity measurements  
34 were conducted using a rotating ring disk electrode (Pine Research Instrument) with a Pt  
35 ring held at 1.2 V vs RHE to measure the H<sub>2</sub>O<sub>2</sub> produced in the reaction. See the SI for  
36 details of ring calibration and selectivity calculations.

## 37 **Computational Details**

1 We performed density functional theory (DFT) calculations using the Vienna Ab Initio  
2 Simulation Package (VASP)<sup>40,41</sup> with the PBE exchange-correlation functional<sup>42</sup> and  
3 projector augmented-wave (PAW) pseudopotentials.<sup>43</sup> We added a Hubbard-U correction  
4 (PBE+U)<sup>44</sup> on insulating Ni oxide materials to include the on-site Coulomb interaction of  
5 localized electrons. The value of the Hubbard interaction, U, for Ni was chosen to be 6.2  
6 eV in accordance with the literature.<sup>45,46</sup> The energy cutoff, convergence criteria for self-  
7 consistent iterations, and for geometry relaxation were set to 500 eV,  $10^{-4}$  eV, 0.05 eV/Å,  
8 respectively. Further computational details can be found in the SI.

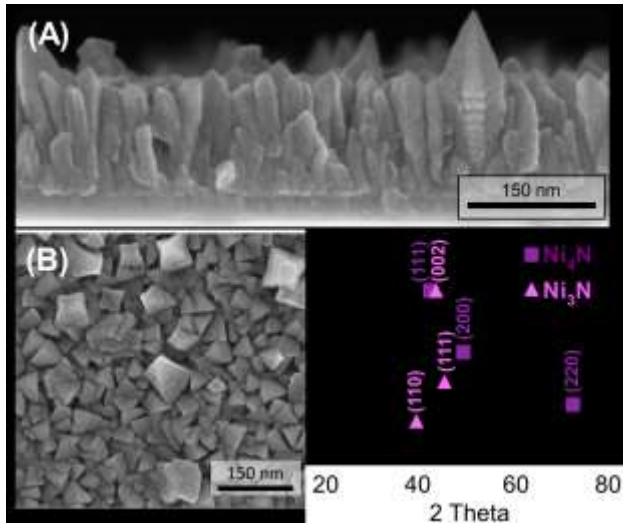
9

## 10 **Results and Discussion**

### 11 **Characterization**

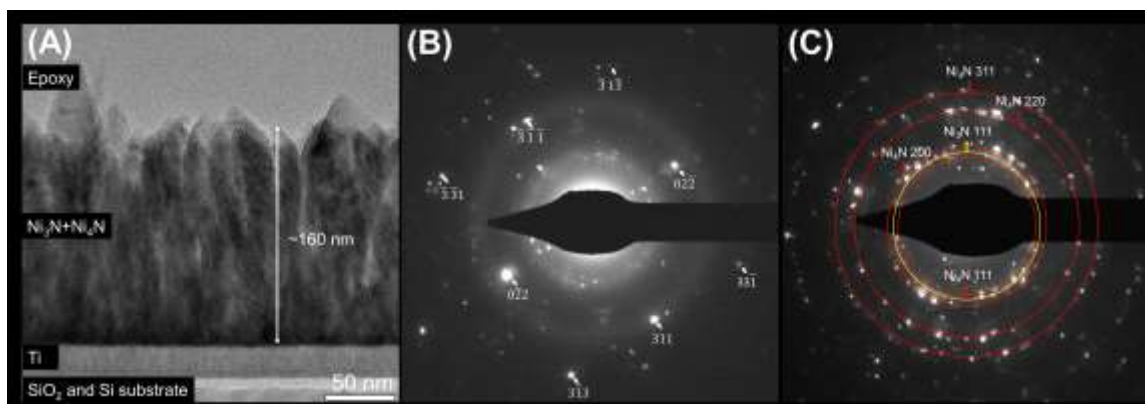
12 The reactively sputtered nickel nitride films are ~160 nm in thickness as shown by cross-  
13 sectional scanning electron microscopy (SEM) in Figure 1A. The film consists of well-  
14 defined nanopillars, which are variable in height but closely packed to form a rough, dense  
15 film. The 20-30 nm Ti sticking layer is visible beneath the pillars. The top down SEM in  
16 Figure 1B shows that the nanopillars are pyramids with either square or triangular base  
17 shapes. The larger square prisms have an average diameter (distance from opposite  
18 corners, viewed from above) of 70 nm, while the triangular prisms are 30-40 nm.

19



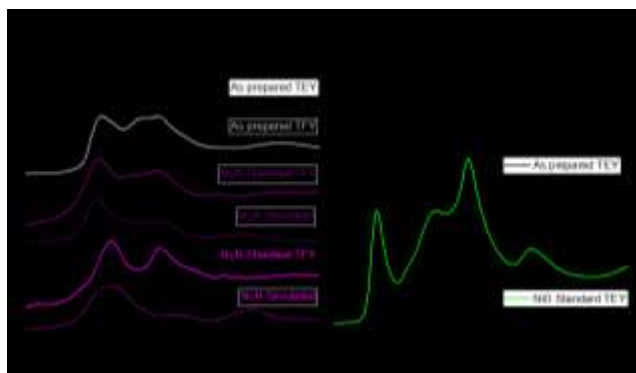
20 **Figure 1.** Characterization of as-prepared, sputtered Ni<sub>x</sub>N thin films. (A) Cross-sectional  
21 and (B) top down SEM micrographs, (C) XRD pattern with ICDD references and  
22 corresponding crystal planes.

23 X-ray diffraction (XRD) of the thin films shows peaks corresponding to both hexagonal  
24 Ni<sub>3</sub>N (ICDD 00-010-0280 at 2 $\Theta$  of 39.9°, 42.7°, and 45.2°) and cubic Ni<sub>4</sub>N (ICDD 00-036-  
25 1300 at 42.0°, 49.3°, and 72.0°), confirming that no other crystalline species are present  
26 (Figure 1C).



1  
2 **Figure 2.** TEM-SADP (selected area diffraction pattern) characterization of as-prepared  
3 Ni<sub>x</sub>N thin films. (A) Cross-sectional view, (B) SADP taken from top surface of the film  
4 matching diffraction pattern of Ni<sub>4</sub>N from  $[\bar{2}33]$  zone axis, (C) SADP taken from the bulk  
5 region of the film showing diffraction rings of Ni<sub>4</sub>N and Ni<sub>3</sub>N.

6  
7 The films were also analyzed using cross-sectional transmission electron microscopy  
8 (TEM). The TEM image of the film in Figure 2A shows a pillar morphology, as seen in  
9 SEM, as well as discrete titanium (20 nm thick), silicon dioxide (7 nm thick), and silicon  
10 layers. Distinct crystalline regions are also visible (Fig. S1). Selected area diffraction  
11 patterns (SADP) were used to determine the crystal structures at the surface and in the  
12 bulk, as shown in Figure 2B and C, respectively. The selected area aperture positions are  
13 shown in Figure S2. In Figure 2B, the diffraction pattern measured at the surface matches  
14 the Ni<sub>4</sub>N cubic structure. The measured d-spacings of diffraction spots along the two  
15 orthogonal directions are 0.131 nm and 0.111 nm. These match well with the (0 $\bar{2}2$ ) and  
16 (311) planes of the reference Ni<sub>4</sub>N. These also suggest that the diffraction pattern was  
17 taken near a  $[\bar{2}33]$  zone axis of Ni<sub>4</sub>N. The diffraction pattern from the bulk region shows  
18 diffraction rings (labeled in red) of Ni<sub>4</sub>N which correspond to the (111), (200), (220), and  
19 (311) planes. This indicates that the bulk of the thin film is polycrystalline. An additional  
20 ring (labeled in yellow) was observed between the (111) and (200) rings of Ni<sub>4</sub>N. The d-  
21 spacing of this ring matches the (111) plane spacing of Ni<sub>3</sub>N. The SADP indicates that  
22 the film is primarily composed of Ni<sub>4</sub>N, with a minor phase of Ni<sub>3</sub>N in the bulk. However,  
23 it is important to note that the analyzed volume of our polycrystalline film from this method  
24 is limited. To probe a broader region of the sample, we employed NEXAFS spectroscopy,  
25 as discussed in the next section.



1  
 2 **Figure 3.** NEXAFS spectra of as-prepared, sputtered Ni<sub>x</sub>N thin films. (A) N K-edge of the  
 3 sample, Ni<sub>3</sub>N and Ni<sub>4</sub>N standards, and simulated spectra; (B) O K-edge of the sample  
 4 and NiO standard. Dashed lines are intended as guides for the reader. TEY: surface;  
 5 TFY: bulk.

6 To further probe the structure and chemical state of the catalyst, the films were  
 7 characterized using NEXAFS spectroscopy. In Figure 3A, the N K-edge NEXAFS spectra  
 8 for the as-prepared catalyst are compared with experimental and simulated spectra for  
 9 Ni<sub>3</sub>N and Ni<sub>4</sub>N standards. The spectra were collected in TEY and TFY modes, allowing  
 10 for a comparison between the surface (TEY: few nm) and the bulk of the film (TFY). Two  
 11 main peaks are present both for the surface and the bulk of the as-prepared sample,  
 12 though differences are evident between the two spectra. For TEY, the feature at 397.5  
 13 eV matches well with both the experimental and simulated spectrum of Ni<sub>4</sub>N. The TFY  
 14 signal shows a shift of the peak at 397.5 eV towards higher energy and the appearance  
 15 of a shoulder corresponding to Ni<sub>3</sub>N. We can thus confirm that the catalyst is a mixture of  
 16 Ni<sub>4</sub>N and Ni<sub>3</sub>N, as indicated by XRD and TEM analyses, and locate Ni<sub>3</sub>N in the bulk. The  
 17 feature at 400.5 eV is associated with the oxidation of the surface of the nitride film upon  
 18 exposure to air after synthesis, as has been previously reported for other transition metal  
 19 nitrides.<sup>47,48</sup> Notably, the fact that the intensity of this feature considerably decreases in  
 20 the bulk of the material provides evidence for the presence of a surface N state different  
 21 than in the pure bulk nitride film. This is also observed in the experimental spectra for the  
 22 Ni<sub>4</sub>N and Ni<sub>3</sub>N standards (Figure S3).

23 Figure 3B shows experimental O K-edge spectra for the catalyst and the NiO standard,  
 24 which allow for further characterization of surface oxidation. The TFY signal for O was  
 25 negligible, confirming that the oxidation process is limited to the surface and there is no  
 26 oxygen incorporation in the bulk. The signal for the oxidized layer on top of the nitride film  
 27 consists of a peak at 532.8 eV, shifted to higher energy compared to the bulk NiO, and a  
 28 broad feature at 540.5 eV, which has been reported for small native Ni oxide clusters on  
 29 top of Ni films.<sup>49</sup> It was concluded that none of the defined features typical of crystalline  
 30 NiO were detected due to the amorphous nature of the small NiO domains. O K-edge  
 31 spectra for NiO clusters of various dimensions were simulated (Fig. S4). The simulated

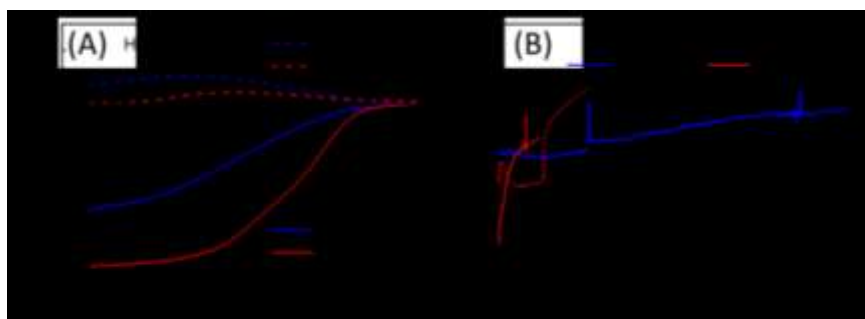


1 spectrum for a NiO cluster with ca. 5 Å radius (57 atom cluster) is the best match to the  
2 experimental, suggesting the presence of these clusters on the nitride surface. The Ni L3-  
3 and L2-edge spectra also support the presence of oxidized Ni<sub>4</sub>N on top of Ni<sub>3</sub>N (Fig. S5).  
4 Our spectroscopic measurements thus indicate that prior to testing, the catalyst structure  
5 consists of small clusters of NiO on top of Ni<sub>4</sub>N, with Ni<sub>3</sub>N crystallites also present in the  
6 bulk.

7

## 8 **Electrochemistry**

9 The ORR activity and selectivity of the nickel nitride catalyst was assessed using a  
10 rotating ring disk electrode (RRDE) in both acidic (0.1 M perchloric acid) and alkaline  
11 (0.1 M potassium hydroxide) electrolyte. Figure 4A shows the activity and selectivity of  
12 the synthesized catalyst, with the ORR polarization curve measured on the disk  
13 electrode (solid lines) and the H<sub>2</sub>O<sub>2</sub> oxidation current measured on the platinum ring  
14 electrode (dashed lines). Comparison with the activity of a commercial Pt/C (46.6% from  
15 TKK) catalyst is shown in Figure S6.<sup>50</sup> In acid, the ORR onsets (defined as the potential  
16 required to reach 100 μA/cm<sup>2</sup> geometric current density) at 0.68 V vs RHE and reaches  
17 the mass transport limited current density of 6.1 mA/cm<sup>2</sup> at 0.2 V vs RHE. Furthermore,  
18 the halfwave potential is 0.49 V vs RHE, indicating a relatively sharp onset. This is  
19 promising activity for a non-Pt group metal catalyst in acid and is comparable to the  
20 metal nitrides currently reported in the literature (Table S3).<sup>51–53</sup> Nickel nitrogen-doped  
21 carbon (Ni-NC) type catalysts have also demonstrated good ORR performance, but  
22 they cannot be directly compared with this work due to their high surface area and the  
23 contributions of the NC support.<sup>54,55</sup> In alkaline electrolyte, nickel nitride shows similar  
24 activity with an onset at 0.68 V vs RHE but has a lower mass transport limited current  
25 density of 4 mA/cm<sup>2</sup>, as well as a slower onset with a halfwave potential of 0.42 V vs  
26 RHE. This difference in activity is reflected in the Tafel slopes: 89.7 mV/decade in acid  
27 compared to 175 mV/decade in alkaline (Fig. S7). Similar pH dependent Tafel slope  
28 trends have been reported in the literature.<sup>56</sup> Aside from the Tafel slopes, PGM-free  
29 catalysts are generally more ORR active in alkaline, with higher onset and halfwave  
30 potentials (Table S3). The reversal in that trend for this nickel nitride system can likely  
31 be attributed to different H<sub>2</sub>O<sub>2</sub> selectivity and different surface structures under reaction  
32 conditions, which will be discussed in the following sections.



1  
 2 **Figure 4.** Electrochemical performance of Ni<sub>x</sub>N in acid (red) and base (blue). (A) RRDE  
 3 measurements showing ORR polarization curves and H<sub>2</sub>O<sub>2</sub> current density for nickel  
 4 nitride. (B) Chronoamperometry (CA) profile at 0.15 V vs RHE in acid, for 2 samples  
 5 tested under different cycling parameters, and in base.

6 For PEMFCs, high selectivity to the 4-electron reduction, corresponding to a low H<sub>2</sub>O<sub>2</sub>  
 7 current, is preferred. In acid, the selectivity of the catalyst to H<sub>2</sub>O<sub>2</sub> (2-electron reduction)  
 8 was found to decrease with increasing overpotential and was negligible at potentials  
 9 below 0.3 V vs RHE. (Fig. S10). The H<sub>2</sub>O<sub>2</sub> current was used to calculate the electron  
 10 transfer number, *n*, which was found to range from 3.2 (at 0.6 V vs RHE) to 4.0 (at 0.1 V  
 11 vs RHE) (see SI for calculations). In alkaline electrolyte, nickel nitride has higher  
 12 selectivity towards H<sub>2</sub>O<sub>2</sub>, with *n* values ranging from 2.4 at 0.6 V vs RHE up to 3.4 at 0.1  
 13 V vs RHE. This high selectivity to H<sub>2</sub>O<sub>2</sub>, as well as the onset of ORR activity close to the  
 14 thermodynamic limiting potential of 0.70 V vs RHE for 2-electron ORR, indicates that in  
 15 alkaline electrolyte the catalyst is unable to turnover 4-electron ORR until the onset of 2-  
 16 electron ORR. This limitation to the thermodynamic potential of 2-electron ORR likely  
 17 contributes to the lower activity in alkaline electrolyte.

18 In addition to activity and selectivity, stability is a crucial performance metric for any  
 19 catalyst. Here, electrochemical stability was assessed using chronoamperometry, and the  
 20 use of post-test characterization and theoretical calculations to evaluate chemical stability  
 21 will be discussed in later sections. Figure 4B shows stability tests for nickel nitride in acid  
 22 and alkaline electrolyte. After 3 CVs, catalyst stability was evaluated by  
 23 chronoamperometry (CA) at 0.15 V vs RHE. CVs were run every 5 h to assess changes  
 24 in activity (Fig. S11).

25 In alkaline, the catalyst improved over the first 5 h of the chronoamperometry hold,  
 26 increasing from 3.3 to 3.5 mA/cm<sup>2</sup> of current density in the CA, and the CV after 5 h  
 27 demonstrated improvement of 25 mV and 75 mV in onset and half-wave potential,  
 28 respectively (Fig. S11B). Subsequent CVs show a slow degradation, with a loss of  
 29 approximately 0.2 mA/cm<sup>2</sup> every 5 h from 10 h to 30 h. The noise in the data, observed  
 30 at 3 h, is due to bubble formation on the surface of the catalyst. The bubble was removed  
 31 mechanically and had no lasting effect on catalyst performance. All other spikes  
 32 correspond to switching between the CA and CVs. The catalyst continued to degrade

1 slowly, with current density losses of 25% at 24 h and 40% at 40 h, at which time the  
2 stability test was ended.

3 Interestingly, in acid, the activity and stability of the nickel nitride catalyst was found to be  
4 dependent on the cycling parameters of the cyclic voltammogram (CV). To illustrate this  
5 dependence, Figure S12 shows cathodic sweeps, with no background subtraction, for  
6 two sibling catalysts in acid. The catalysts were tested identically, except that the sweeps  
7 started either at more positive (0.8 V vs RHE), as was shown in Figure 4A, or less positive  
8 (0.15 V vs RHE) potential. The “more positive start” catalyst shows superior activity, with  
9 both an earlier onset and larger limiting current density. However, it loses activity more  
10 rapidly, producing only 3 mA/cm<sup>2</sup> after 5 h, corresponding to a 50% loss in activity. CVs  
11 during the stability test for the “less positive start” catalyst are shown in Figure S11A, with  
12 relatively similar ORR activity at 0 and 5 h, but a significant loss of activity during the cycle  
13 at 10 h. These differences in activity and stability between these testing protocols, as well  
14 as the losses caused by the CVs during the CA, provide evidence that the catalyst is very  
15 sensitive to applied potential.

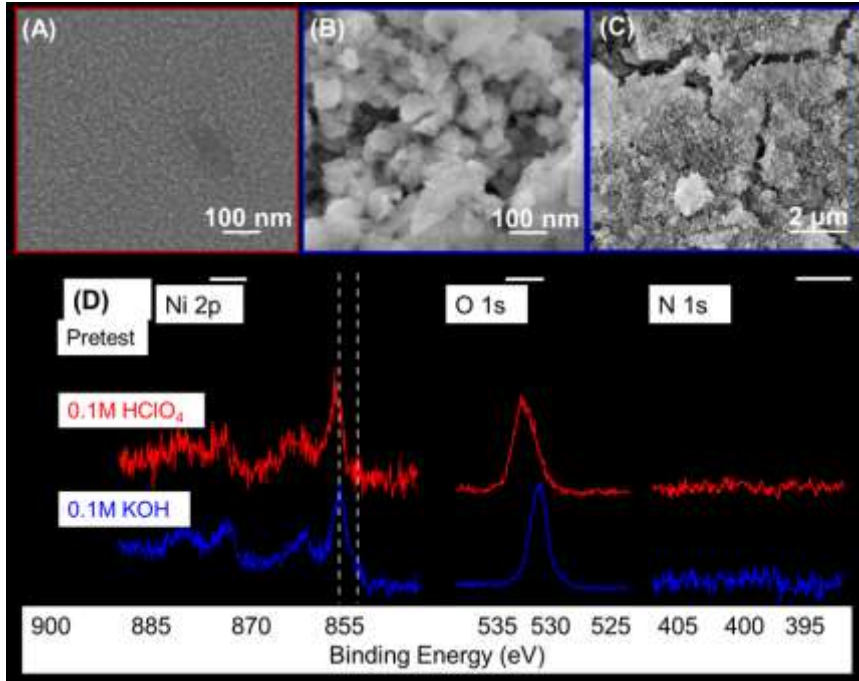
16 Sensitivity to potential is likely a consequence of surface oxidation reactions which occur  
17 in the ORR potential window.<sup>57</sup> In both N<sub>2</sub> and O<sub>2</sub> scans, there was an irreversible  
18 oxidative peak on the anodic sweep in the 0.65 – 0.8 V vs RHE region during the first 4  
19 sweeps (Figure S13). Between sweeps 1 and 3, this results in a positive shift in onset  
20 potential by 100 mV and a 2 mA/cm<sup>2</sup> gain in mass transport limited-current density. This  
21 oxidation peak shrinks after 4 sweeps, indicating that further oxidation of the catalyst was  
22 limited. This coincided with a loss of activity, with current density decreasing to zero over  
23 the subsequent 4 sweeps. We therefore hypothesize that the active surface is a partially  
24 oxidized nitride and that the activity is suppressed, as the oxidation progresses, through  
25 decreased conductivity and dissolution. This reveals the sensitivity of the catalyst to open  
26 circuit potential and oxidizing potentials; durability could be improved by maintaining the  
27 catalyst at reducing currents.

28

## 29 **Characterization After Electrochemical Testing**

30 To better understand chemical stability and investigate the mechanisms of failure in acid  
31 and base, the films were characterized after activity (CV) and stability (CA) testing using  
32 SEM and XPS. After the 10 h CA in acid (Figure 5A), SEM shows that the surface  
33 structure had changed completely, with most of the material gone. This structural change  
34 likely contributes to the loss in performance over time. After the 40 h CA in base (Figure  
35 5B,C), the structure is distinct from the as-prepared catalyst. The surface was covered  
36 with rod-shaped structures, loosely packed into clusters approximately 0.1 μm<sup>2</sup> in area,  
37 and large cracks (approximately 300 nm across) appeared in the film. We hypothesize

1 that these cracks may have undercut the film, disturbing its electrical connectivity and  
2 performance.



3  
4 **Figure 5.** Top down SEM images of the nickel nitride films after (A) stability test in acid,  
5 and (B, C) stability test in base. (D) High-resolution XPS spectra for as-prepared (black),  
6 post-stability acid (red), and post-stability base (blue) for Ni 2p, O 1s, and N 1s regions.  
7 Dashed lines are intended as guides for the reader.

8  
9 The XPS spectra (Figure 5D) also show a change in elemental composition. Before  
10 continuing with this discussion, it is necessary to note that accurate quantitative analysis  
11 of this XPS data is difficult due to the complexity of the Ni 2p spectrum, so all statements  
12 of composition are meant as best approximation. Elemental quantification of the nickel  
13 nitride revealed a ratio of Ni to N of approximately 3.5, consistent with a mixture of Ni<sub>3</sub>N  
14 and Ni<sub>4</sub>N observed in XRD. Prior to testing, peaks were identified in the Ni 2p<sub>3/2</sub> region at  
15 binding energies of 853.0 and 855.2 eV (dashed lines), corresponding to the interstitial  
16 nitride (Ni<sup>δ+</sup>, δ = 0-2) and oxide (Ni<sup>2+</sup>), respectively. There are satellite peaks in the region  
17 860 – 865 eV. This matches well with literature spectra for nickel nitride.<sup>58</sup> In the O 1s  
18 region, the low energy peak at 529.3 eV corresponds to the nickel oxide, while we  
19 associate the higher energy peak with hydroxide (literature value of 531.1 eV) and  
20 carbonyl species (most likely carbonate, literature value of 532.8 eV).<sup>59</sup> Finally, the N 1s  
21 peak at 397.6 eV corresponds to a metal nitride.

22 After stability testing in acid, the surface composition changed drastically. The Ni 2p<sub>3/2</sub>  
23 peaks shifted to higher binding energies, with the largest peak at 855.8 eV, indicating the

1 Ni<sup>2+</sup> oxidation state. The N 1s peak disappeared, corresponding to a loss of nitrogen from  
2 the surface. The O 1s peaks increased in intensity relative to the Ni and indicate the  
3 presence of hydroxide and carbonate species (from air exposure prior to  
4 characterization).<sup>60</sup> In conjunction with the structural changes observed by SEM, this  
5 indicates an extensive reorganization of the surface during testing, resulting in a surface  
6 that more closely resembles Ni(OH)<sub>2</sub> than the original Ni<sub>4</sub>N.<sup>61</sup> Similar composition  
7 changes were observed after CV testing in acid (Figure S14). From XPS it is not possible  
8 to determine when these changes occurred, though it seems likely that they were caused  
9 by exposure to oxidizing potentials during testing or open circuit potential when the  
10 catalyst is removed from electrolyte. These structural and composition changes indicate  
11 that overall chemical stability is poor in acid. However, an analysis of potential corrosion  
12 current, as well as the poor ORR activity of the underlying Ti and glassy carbon in acid,  
13 indicates that the Ni<sub>x</sub>N catalyst is responsible for the current observed during the stability  
14 test (see SI for details).

15 The composition change after stability testing in base is similar. The primary remaining  
16 Ni 2p<sub>3/2</sub> peak is at 855.9 eV and there is no N 1s signal at the surface, indicating a  
17 complete conversion at the surface to a hydroxide structure. The O 1s spectrum shows a  
18 small oxide peak, but hydroxide is the dominant species. Comparatively, the composition  
19 changes after CV testing are minor, with nitride composition retained (Fig. S14). This was  
20 confirmed by the bulk NEXAFS spectra, which showed no significant change between  
21 this and the as-deposited sample (Fig. S15). This electrochemical, microscopic, and  
22 spectroscopic investigation of stability and failure mechanisms has revealed that activity  
23 loss is correlated with the conversion of the nitride to hydroxide and associated material  
24 property changes. Due to the sensitivity of the activity and stability of these catalysts to  
25 applied potential, future work should focus on probing the stability of these catalysts as a  
26 function of applied potential. We hypothesize that stability would be more challenging at  
27 more oxidizing conditions, since extensive catalyst oxidation was found to detrimentally  
28 impact activity and stability.

29 To gain insight into oxide phases observed experimentally, we evaluated the stability of  
30 oxide phases in the presence of Ni<sub>3</sub>N and Ni<sub>4</sub>N with DFT. The optimized bulk structures  
31 of Ni<sub>3</sub>N and Ni<sub>4</sub>N are in good agreement with the XRD and SADP results, as well as  
32 previously reported bulk parameters (a=b=4.619 and c=4.307 Å for Ni<sub>3</sub>N, a=b=c=3.730 Å  
33 for Ni<sub>4</sub>N).<sup>62,63</sup> We modeled  $\sqrt{3} \times \sqrt{3}$  structures for Ni<sub>3</sub>N (0001) and Ni<sub>4</sub>N (111) to minimize  
34 the lattice mismatch between nickel nitrides (Ni<sub>3</sub>N and Ni<sub>4</sub>N) and nickel oxides (NiOOH  
35 and NiO). In the next step we simulated monolayer films of NiOOH and NiO supported on  
36 Ni<sub>3</sub>N and Ni<sub>4</sub>N (Figure 6A). We considered all possible adsorption sites and surface  
37 termination to minimize the oxide nitride interface formation energy. The formation  
38 energies of nickel oxides films (NiOOH and NiO) on nickel nitrides (Ni<sub>3</sub>N and Ni<sub>4</sub>N) are  
39 calculated as following:

$$E_{\text{Formation}} = [E_{\text{slab,oxide+nitride}} - E_{\text{slab,nitride}} - nE_{\text{bulk,oxide}}]/n,$$

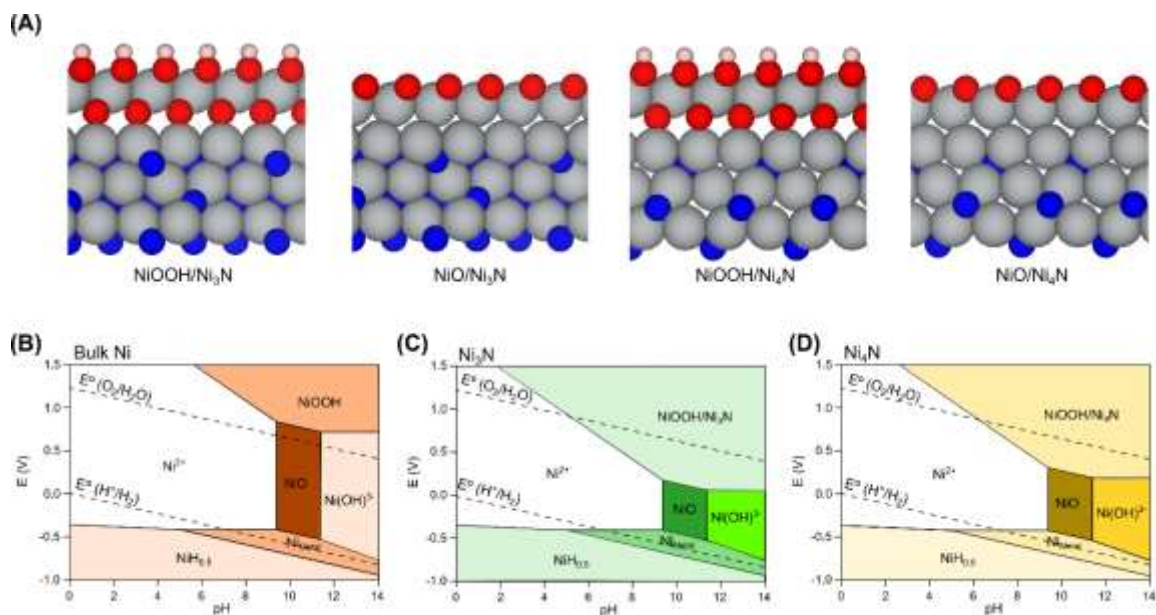
Where  $E_{\text{slab,oxide+nitride}}$ ,  $E_{\text{slab,nitride}}$  and  $E_{\text{bulk,nitride}}$  are electronic energies of the total system, slab structure of nitrides and bulk nickel oxides. The  $n$  is the number of oxide units in the total system. The most stable geometries for NiOOH and NiO on Ni<sub>3</sub>N and Ni<sub>4</sub>N are shown in Figure 6A and Table 1 summarizes the results of formation energy calculations. These results show that NiOOH layer is effectively stabilized by -0.67 and -0.53 eV/f.u on Ni<sub>3</sub>N and Ni<sub>4</sub>N, respectively, while NiO is significantly destabilized.

**Table 1.** The calculated formation energy of Ni oxide species on Ni nitrides.

Formation energy (eV/f.u.)	Ni <sub>3</sub> N	Ni <sub>4</sub> N
NiOOH	-0.67	-0.53
NiO	1.60	1.64

10

To further elaborate the formation of different oxide phases during ORR testing, as well as differences in stability between acid and alkaline electrolyte, we constructed Pourbaix diagrams. Figure 6 shows (A) the most stable geometries of the NiO and NiOOH overlayers as well as the theoretically calculated Pourbaix diagrams for (B) bulk Ni, (C) Ni<sub>3</sub>N, and (D) Ni<sub>4</sub>N. The region of interest for ORR is 0.2 V<sub>RHE</sub> to 1.23 V<sub>RHE</sub>, below the upper dashed line in the Pourbaix diagram. The strong formation energy of NiOOH on both Ni<sub>3</sub>N and Ni<sub>4</sub>N results in the expansion of NiOOH area in the Pourbaix diagrams (Fig 6C and D). Hence, the observed oxidized phase in the experiment can be attributed to the stabilized NiOOH on the nickel nitride surfaces, particularly in alkaline electrolyte. This analysis also shows that nickel nitride surfaces are not stable under acidic environment due to dissolution of Ni<sup>2+</sup> ions. Differences in surface composition and coverage between these electrolytes may contribute to the observed differences in ORR activity and selectivity.



1  
 2 **Figure 6.** (A) Optimized geometries of NiO and NiOOH supported on Ni<sub>3</sub>N and Ni<sub>4</sub>N,  
 3 respectively. Pourbaix diagrams of (B) bulk Ni, (C) Ni<sub>3</sub>N, and (D) Ni<sub>4</sub>N. (B) is based on  
 4 the experimental values of formation free energies of bulk phases<sup>62,63</sup>, and the  
 5 stabilization energies of nickel nitrides on NiOOH were added to construct (C) and (D).  
 6 NiO is destabilized on the nickel nitrides, thus the bulk formation free energy was used.  
 7 Color codes: silver (Ni), blue (N), red (O), pink (H). The equilibrium potentials of O<sub>2</sub>/H<sub>2</sub>O  
 8 (1.23 V<sub>RHE</sub>) and H<sup>+</sup>/H<sub>2</sub> (0.00 V<sub>RHE</sub>) are marked with dashed lines.

9 The above theoretical investigation provides a basic understanding of the formation of  
 10 possible nickel oxide phases on the examined nickel nitrides, which is of particular interest  
 11 due to recent DFT calculations showing that the formation of an oxide over-layer on cobalt  
 12 nitride promotes ORR.<sup>64</sup> This is in agreement with our experimental observation of  
 13 extensive surface oxidation after ORR testing. While the XPS and NEXAFS results  
 14 indicate a surface hydroxide species, these are *ex situ* measurements, taken after the  
 15 catalysts had been exposed to air, and thus cannot be used to determine the surface  
 16 composition under reaction conditions. This will be the subject of future investigations  
 17 utilizing operando spectroscopies.

18 It is important to note that the Pourbaix diagram is based on thermodynamics and does  
 19 not provide any information about the kinetics of the phase transition. Thus, while the  
 20 nickel nitride is not predicted to be stable in acid, several hours of stability were achieved,  
 21 perhaps because the oxidation or dissolution processes are slow kinetically. This can  
 22 serve as a design principle for further catalyst development. Superior stability is observed  
 23 in base, where the catalyst is more thermodynamically stable.

24 The use of a well-defined and carbon-free catalyst morphology facilitated a combined  
 25 experiment-theory approach to determining the active surface of the catalyst. With the

1 insights into the origins of activity and stability obtained through the study of this model  
2 system, efforts to improve this catalyst fall into two main categories.<sup>65</sup> First, intrinsic  
3 activity and stability can be improved through alloying with a more stable transition metal  
4 nitride, which has been demonstrated for several nitride systems.<sup>22,23,29</sup> Based on the  
5 Pourbaix calculations and the potential of activation via oxide over-layer formation,<sup>64</sup> a  
6 promising candidate would be a metal nitride which forms a stable, passivating oxide or  
7 hydroxide surface in acid and alkaline electrolyte. Second, after discovery of a promising  
8 material system, the number of active sites can be increased through nanostructuring and  
9 supporting the catalyst on a high surface area material such as N-doped carbon.<sup>54,55</sup>

10

## 11 **Conclusions**

12 In summary, nickel nitride thin films were found to be active ORR catalysts, achieving  
13 activity comparable to the metal nitrides reported in the literature. Reactive sputtering is  
14 highlighted as a promising route to synthesize transition metal nitride electrocatalysts with  
15 a variety of compositions and crystal structures, allowing for fundamental investigation of  
16 the active surface. By synthesizing the catalyst in a carbon-free morphology, we were  
17 able to use a combined experiment-theory approach to isolate the activity of the nickel  
18 nitride and found that it is an active and reasonably stable non-precious metal catalyst for  
19 ORR in acid, as well as in base. In future work, catalyst activity and stability could be  
20 improved through alloying and nanostructuring. *Ex situ* XAS and XPS characterization  
21 indicated that an oxide overlayer readily forms on the catalyst surface. DFT calculations  
22 predicted similar surface oxidation under reaction conditions, which was shown to  
23 correlate with changes in electrochemical activity and stability. This surface oxidation can  
24 serve as a design principle for a variety of metal nitride catalysts and demonstrates the  
25 importance of complementary experimental and theoretical studies.

26

## 27 **Associated Content**

28 Supporting Information available: Supplementary experimental characterization (TEM,  
29 XRD, NEXAFS, electrochemistry, and XPS), and details for H<sub>2</sub>O<sub>2</sub> selectivity, Tafel, and  
30 TOF calculations. Raw data from all main text figures are also provided, in line with the  
31 U.S. Department of Energy requirements.

32

## 33 **Author Information & Notes**

34 Corresponding Authors:

35 \*Email: [lking10@stanford.edu](mailto:lking10@stanford.edu)

36 \*Email: [jaramillo@stanford.edu](mailto:jaramillo@stanford.edu)



1 ORCID  
2 Melissa E. Kreider 0000-0003-1750-6860  
3 Yunzhi Liu 0000-0003-0524-4023  
4 Seoin Back: 0000-0003-4682-0621  
5 Samira Siahrostami: 0000-0002-1192-4634  
6 Dennis Nordlund: 0000-0001-9524-6908  
7 Laurie A. King: 0000-0002-0772-2378  
8 Thomas F. Jaramillo: 0000-0001-9900-0622

9 Notes

10 The authors declare no competing financial interest.

## 11 **Acknowledgement**

12 The authors gratefully acknowledge the support of the Toyota Research Institute. The US  
13 Department of Energy (DoE) Office of Basic Energy Sciences (BES) is gratefully  
14 acknowledged for primary support for SUNCAT Center for Interface Science and  
15 Catalysis. Part of this work was performed at the Stanford Nano Shared Facilities (SNSF)  
16 and the Stanford Nanofabrication Facility (SNF), supported by the National Science  
17 Foundation under Award ECCS-1542152. Use of the Stanford Synchrotron Radiation  
18 Lightsource, SLAC National Accelerator Laboratory, is supported by the U.S. Department  
19 of Energy, Office of Science, Office of Basic Energy Sciences under Contract No. DE-  
20 AC02-76SF00515. This research used resources of the National Energy Research  
21 Scientific Computing Center (NERSC), a U.S. Department of Energy Office of Science  
22 User Facility operated under Contract No. DE-AC02-05CH11231. AG would like to thank  
23 J. Vinson at NIST for his support with the OCEAN code.

24

## 25 **References**

- 26 (1) Ramaswamy, N.; Mukerjee, S. Fundamental Mechanistic Understanding of  
27 Electrocatalysis of Oxygen Reduction on Pt and Non-Pt Surfaces: Acid versus  
28 Alkaline Media. *Adv. Phys. Chem.* **2012**, *2012*, 1–17.
- 29 (2) Gasteiger, H. A.; Kocha, S. S.; Sompalli, B.; Wagner, F. T. Activity Benchmarks  
30 and Requirements for Pt, Pt-Alloy, and Non-Pt Oxygen Reduction Catalysts for  
31 PEMFCs. *Appl. Catal. B Environ.* **2005**, *56*, 9–35.
- 32 (3) Rabis, A.; Rodriguez, P.; Schmidt, T. J. Electrocatalysis for Polymer Electrolyte  
33 Fuel Cells : Recent Achievements and Future Challenges. *ACS Catal.* **2012**, *2*,  
34 864–890.
- 35 (4) Greeley, J.; Stephens, I. E. L.; Bondarenko, A. S.; Johansson, T. P.; Hansen, H.  
36 A.; Jaramillo, T. F.; Rossmeisl, J.; Chorkendorff, I.; Nørskov, J. K. Alloys of

- 1 Platinum and Early Transition Metals as Oxygen Reduction Electrocatalysts. *Nat.*  
2 *Chem.* **2009**, *1*, 552–556.
- 3 (5) Stamenkovic, V. R.; Fowler, B.; Mun, B. S.; Wang, G.; Ross, P. N.; Lucas, C. A.;  
4 Markovic, N. M. Improved Oxygen Reduction Activity on Pt<sub>3</sub>Ni(111) via Increased  
5 Surface Site Availability. *Science* **2007**, *315* (5811), 493–498.
- 6 (6) Chen, S.; Sheng, W.; Yabuuchi, N.; Ferreira, P. J.; Allard, L. F. Origin of Oxygen  
7 Reduction Reaction Activity on “Pt<sub>3</sub>Co” Nanoparticles: Atomically Resolved  
8 Chemical Compositions and Structures. *J. Phys. Chem. C* **2009**, *113*, 1109–1125.
- 9 (7) Zhou, M.; Wang, H.; Elnabawy, A. O.; Hood, Z. D.; Chi, M.; Xiao, P.; Zhang, Y.;  
10 Mavrikakis, M.; Xia, Y. Facile One-Pot Synthesis of Pd@Pt 1L Octahedra with  
11 Enhanced Activity and Durability toward Oxygen Reduction. *Chem. Mater.* **2019**,  
12 *31* (4), 1370–1380.
- 13 (8) Jaouen, F.; Proietti, E.; Lefevre, M.; Chenitz, R.; Dodelet, J.-P.; Wu, G.; Chung, H.  
14 T.; Johnston, C. M.; Zelenay, P. Recent Advances in Non-Precious Metal  
15 Catalysis for Oxygen-Reduction Reaction in Polymer Electrolyte Fuel Cells.  
16 *Energy Environ. Sci.* **2011**, *4*, 114–130.
- 17 (9) Shinozaki, K.; Zack, J. W.; Richards, R. M.; Pivovar, B. S.; Kocha, S. S. Oxygen  
18 Reduction Reaction Measurements on Platinum Electrocatalysts Utilizing Rotating  
19 Disk Electrode Technique. *J. Electrochem. Soc.* **2015**, *162* (10), F1144–F1158.
- 20 (10) Camara, G. A.; Ticianelli, E. A.; Mukerjee, S.; Lee, S. J.; Mcbreen, J. The CO  
21 Poisoning Mechanism of the Hydrogen Oxidation Reaction in Proton Exchange  
22 Membrane Fuel Cells. *J. Electrochem. Soc.* **2002**, *149* (6), 748–753.
- 23 (11) Suntivich, J.; Gasteiger, H. A.; Yabuuchi, N.; Nakanishi, H.; Goodenough, J. B.;  
24 Shao-Horn, Y. Design Principles for Oxygen-Reduction Activity on Perovskite  
25 Oxide Catalysts for Fuel Cells and Metal-Air Batteries. *Nat. Chem.* **2011**, *3* (7),  
26 546–550.
- 27 (12) Stoerzinger, K. A.; Li, C.; Venkatesan, T.; Shao-Horn, Y. Highly Active Epitaxial  
28 La(1-x)SrxMnO<sub>3</sub> Surfaces for the Oxygen Reduction Reaction: Role of Charge  
29 Transfer. *J. Phys. Chem. Lett.* **2015**, *6*, 1435–1440.
- 30 (13) Wei, W.; Liang, H.; Parvez, K.; Zhuang, X.; Feng, X.; Müllen, K. Nitrogen-Doped  
31 Carbon Nanosheets with Size-Defined Mesopores as Highly Efficient Metal-Free  
32 Catalyst for the Oxygen Reduction Reaction. *Angew. Chemie* **2014**, *126*, 1596–  
33 1600.
- 34 (14) Ratso, S.; Sahraie, N. R.; Sougrati, M. T.; Kaarik, M.; Kook, M.; Saar, R.; Paiste,  
35 P.; Jia, Q.; Leis, J.; Mukerjee, S.; Jaouen, F.; Tammeveski, K. Synthesis of  
36 Highly-Active Fe – N – C Catalysts for PEMFC with Carbide-Derived Carbons. *J.*  
37 *Mater. Chem. A* **2018**, *6*, 14663–14674.
- 38 (15) Shao, Y.; Sui, J.; Yin, G.; Gao, Y. Nitrogen-Doped Carbon Nanostructures and  
39 Their Composites as Catalytic Materials for Proton Exchange Membrane Fuel  
40 Cell. *Appl. Catal. B Environ.* **2008**, *79*, 89–99.

- 1 (16) Chung, H. T.; Cullen, D. A.; Higgins, D.; Sneed, B. T.; Holby, E. F.; More, K. L.;  
2 Zelenay, P. Direct Atomic-Level Insight into the Active Sites of a High-  
3 Performance PGM-Free ORR Catalyst. *Science* **2017**, *357*, 479–484.
- 4 (17) Dong, S.; Chen, X.; Zhang, X.; Cui, G. Nanostructured Transition Metal Nitrides  
5 for Energy Storage and Fuel Cells. *Coord. Chem. Rev.* **2013**, *257* (13–14), 1946–  
6 1956.
- 7 (18) Oyama, S. T. Preparation and Catalytic Properties of Transition Metal Carbides  
8 and Nitrides. *Catal. Today* **1992**, *15* (2), 179–200.
- 9 (19) An, L.; Huang, W.; Zhang, N.; Chen, X.; Xia, D. A Novel CoN Electrocatalyst with  
10 High Activity and Stability toward Oxygen Reduction Reaction. *J. Mater. Chem. A*  
11 **2014**, *2*, 62–65.
- 12 (20) Liu, M.; Dong, Y.; Wu, Y.; Feng, H.; Li, J. Titanium Nitride Nanocrystals on  
13 Nitrogen-Doped Graphene as an Efficient Electrocatalyst for Oxygen Reduction  
14 Reaction. *Chem. - A Eur. J.* **2013**, *19* (44), 14781–14786.
- 15 (21) Yang, W.; Rehman, S.; Chu, X.; Hou, Y.; Gao, S. Transition Metal (Fe, Co and Ni)  
16 Carbide and Nitride Nanomaterials: Structure, Chemical Synthesis and  
17 Applications. *ChemNanoMat* **2015**, *1* (6), 376–398.
- 18 (22) Tian, X. L.; Wang, L.; Chi, B.; Xu, Y.; Zaman, S.; Qi, K.; Liu, H.; Liao, S.; Xia, B. Y.  
19 Formation of a Tubular Assembly by Ultrathin Ti<sub>0.8</sub>Co<sub>0.2</sub>N Nanosheets as  
20 Efficient Oxygen Reduction Electrocatalysts for Hydrogen-/Metal-Air Fuel Cells.  
21 *ACS Catal.* **2018**, *8*, 8970–8975.
- 22 (23) Tian, X.; Luo, J.; Nan, H.; Fu, Z.; Zeng, J.; Liao, S. Binary Transition Metal  
23 Nitrides with Enhanced Activity and Durability for the Oxygen Reduction Reaction.  
24 *J. Mater. Chem. A* **2015**, *3* (32), 16801–16809.
- 25 (24) Vaughn, D. D.; Araujo, J.; Meduri, P.; Callejas, J. F.; Hickner, M. A.; Schaak, R. E.  
26 Solution Synthesis of Cu<sub>3</sub>PdN Nanocrystals as Ternary Metal Nitride  
27 Electrocatalysts for the Oxygen Reduction Reaction. *Chem. Mater.* **2014**, *26* (21),  
28 6226–6232.
- 29 (25) Ningthoujam, R. S.; Gajbhiye, N. S. Synthesis, Electron Transport Properties of  
30 Transition Metal Nitrides and Applications. *Prog. Mater. Sci.* **2015**, *70*, 50–154.
- 31 (26) Wang, T.; Yan, Z.; Michel, C.; Pera-Titus, M.; Sautet, P. Trends and Control in the  
32 Nitridation of Transition-Metal Surfaces. *ACS Catal.* **2017**, 63–68.
- 33 (27) Chen, W.-F.; Muckerman, J. T.; Fujita, E. Recent Developments in Transition  
34 Metal Carbides and Nitrides as Hydrogen Evolution Electrocatalysts. *Chem.*  
35 *Commun.* **2013**, *49* (79), 8896–8909.
- 36 (28) Sun, T.; Wu, Q.; Che, R.; Bu, Y.; Jiang, Y.; Li, Y.; Yang, L.; Wang, X.; Hu, Z.  
37 Alloyed Co-Mo Nitride as High-Performance Electrocatalyst for Oxygen Reduction  
38 in Acidic Medium. *ACS Catal.* **2015**, *5* (3), 1857–1862.
- 39 (29) Cao, B.; Neufeind, J. C.; Adzic, R. R.; Khalifah, P. G. Molybdenum Nitrides as

- 1 Oxygen Reduction Reaction Catalysts: Structural and Electrochemical Studies.  
2 *Inorg. Chem.* **2015**, *54* (5), 2128–2136.
- 3 (30) Huang, Q.; Chen, S.; Ma, T.; Zou, H.; Yang, W. TiN Supported Cobalt and  
4 Molybdenum Nitrides as an Efficient Oxygen Reduction Reaction Catalyst in Acid  
5 Medium. *Int. J. Electrochem. Sci.* **2017**, *12* (7), 6340–6351.
- 6 (31) Shalom, M.; Ressnig, D.; Yang, X.; Clavel, G.; Fellingner, T. P.; Antonietti, M.  
7 Nickel Nitride as an Efficient Electrocatalyst for Water Splitting. *J. Mater. Chem. A*  
8 **2015**, *3* (15), 8171–8177.
- 9 (32) Fan, Y.; Ida, S.; Staykov, A.; Akbay, T.; Hagiwara, H.; Matsuda, J.; Kaneko, K.;  
10 Ishihara, T. Ni-Fe Nitride Nanoplates on Nitrogen-Doped Graphene as a  
11 Synergistic Catalyst for Reversible Oxygen Evolution Reaction and Rechargeable  
12 Zn-Air Battery. *Small* **2017**, *13* (25), 1–8.
- 13 (33) Fu, G.; Cui, Z.; Chen, Y.; Xu, L.; Tang, Y.; Goodenough, J. B. Hierarchically  
14 Mesoporous Nickel-Iron Nitride as a Cost-Efficient and Highly Durable  
15 Electrocatalyst for Zn-Air Battery. *Nano Energy* **2017**, *39* (June), 77–85.
- 16 (34) Cui, Z.; Fu, G.; Li, Y.; Goodenough, J. B. Ni<sub>3</sub>FeN-Supported Fe<sub>3</sub>Pt Intermetallic  
17 Nanoalloy as a High-Performance Bifunctional Catalyst for Metal–Air Batteries.  
18 *Angew. Chemie - Int. Ed.* **2017**, *56* (33), 9901–9905.
- 19 (35) Zhang, H.; Liu, M.; Cheng, W.; Li, Y.; Zhou, W.; Su, H.; Zhao, X.; Yao, P.; Liu, Q.  
20 Metallic Ni<sub>3</sub>N Quantum Dots as Synergistic Promoter for NiO Nanosheet towards  
21 Efficient Oxygen Reduction Electrocatalysis. *J. Phys. Chem. C* **2019**, *123* (14),  
22 8633–8639.
- 23 (36) Bravman, J. C.; Sinclair, R. The Preparation of Cross-Section Specimens for  
24 Transmission Electron Microscopy. *J. Electron Microsc. Tech.* **1984**, *1*, 53–61.
- 25 (37) Gilmore, K.; Vinson, J.; Shirley, E. L.; Prendergast, D.; Pemmaraju, C. D.; Kas, J.  
26 J.; Vila, F. D.; Rehr, J. J. Efficient Implementation of Core-Excitation Bethe  
27 Salpeter Equation Calculations. *Comput. Phys. Commun.* **2015**, *197*, 109–117.
- 28 (38) Vinson, J.; Rehr, J. J.; Kas, J. J.; Shirley, E. L. Bethe-Salpeter Equation  
29 Calculations of Core Excitation Spectra. *Phys. Rev. B - Condens. Matter Mater.*  
30 *Phys.* **2011**, *83* (11), 115106.
- 31 (39) Rehr, J. J.; Kas, J. J.; Vila, F. D.; Prange, M. P.; Jorissen, K. Parameter-Free  
32 Calculations of X-Ray Spectra with FEFF9. *Phys. Chem. Chem. Phys.* **2010**, *12*  
33 (21), 5503–5513.
- 34 (40) Joubert, D. From Ultrasoft Pseudopotentials to the Projector Augmented-Wave  
35 Method. *Phys. Rev. B - Condens. Matter Mater. Phys.* **1999**, *59* (3), 1758–1775.
- 36 (41) Kresse, G.; Furthmüller, J. Efficiency of Ab-Initio Total Energy Calculations for  
37 Metals and Semiconductors Using a Plane-Wave Basis Set. *Comput. Mater. Sci.*  
38 **1996**, *6*, 15–50.
- 39 (42) Hammer, B.; Hansen, L. B.; Nørskov, J. K. Improved Adsorption Energetics within

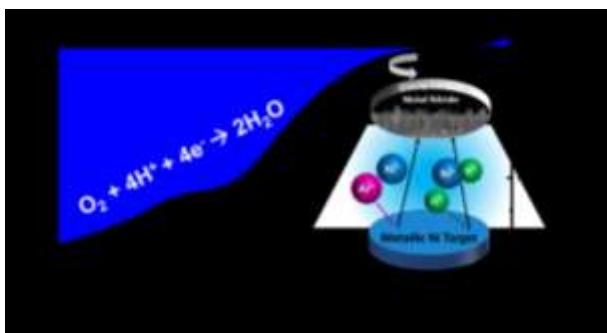
- 1 Density-Functional Theory Using Revised Perdew-Burke-Ernzerhof Functionals.  
2 *Phys. Rev. B - Condens. Matter Mater. Phys.* **1999**, *59* (11), 7413–7421.
- 3 (43) Blöchl, P. E. Projector Augmented-Wave Method. *Phys. Rev. B* **1994**, *50* (24),  
4 17953–17979.
- 5 (44) Dudarev, S.; Botton, G. Electron-Energy-Loss Spectra and the Structural Stability  
6 of Nickel Oxide: An LSDA+U Study. *Phys. Rev. B - Condens. Matter Mater. Phys.*  
7 **1998**, *57* (3), 1505–1509.
- 8 (45) Wang, L.; Maxisch, T.; Ceder, G. Oxidation Energies of Transition Metal Oxides  
9 within the GGA+U Framework. *Phys. Rev. B - Condens. Matter Mater. Phys.*  
10 **2006**, *73*, 195107.
- 11 (46) Jain, A.; Hautier, G.; Ong, S. P.; Moore, C. J.; Fischer, C. C.; Persson, K. A.;  
12 Ceder, G. Formation Enthalpies by Mixing GGA and GGA + U Calculations. *Phys.*  
13 *Rev. B - Condens. Matter Mater. Phys.* **2011**, *84* (4), 1–10.
- 14 (47) Fioretti, A. N.; Schwartz, C. P.; Vinson, J.; Nordlund, D.; Prendergast, D.;  
15 Tamboli, A. C.; Caskey, C. M.; Tuomisto, F.; Linez, F.; Christensen, S. T.; Toberer  
16 E.S.; Lany, S.; Zakutayev, A. Understanding and Control of Bipolar Doping in  
17 Copper Nitride. *J. Appl. Phys.* **2016**, *119* (18), 181508.
- 18 (48) Esaka, F.; Furuya, K.; Shimada, H.; Imamura, M.; Matsubayashi, N.; Sato, H.;  
19 Nishijima, A.; Kawana, A.; Ichimura, H.; Kikuchi, T. Comparison of Surface  
20 Oxidation of Titanium Nitride and Chromium Nitride Films Studied by X-Ray  
21 Absorption and Photoelectron Spectroscopy. *J. Vac. Sci. Technol. A Vacuum,*  
22 *Surfaces, Film.* **1997**, *15* (5), 2521–2528.
- 23 (49) Chen, J. G.; Fischer, D. A.; Hardenbergh, J. H.; Hall, R. B. A Fluorescence-Yield  
24 near-Edge Spectroscopy (FYNES) Investigation of the Reaction Kinetics of  
25 NiO/Ni(100) with Hydrogen. *Surf. Sci.* **1992**, *279* (1–2), 13–22.
- 26 (50) Jackson, A.; Strickler, A.; Higgins, D.; Jaramillo, T. F. Engineering Ru @ Pt Core-  
27 Shell Catalysts for Enhanced Electrochemical Oxygen Reduction Mass Activity  
28 and Stability. *Nanomaterials* **2018**, *8*, 38–52.
- 29 (51) Luo, J.; Tian, X.; Zeng, J.; Li, Y.; Song, H.; Liao, S. Limitations and Improvement  
30 Strategies for Early-Transition-Metal Nitrides as Competitive Catalysts toward the  
31 Oxygen Reduction Reaction. *ACS Catal.* **2016**, *6*, 6165–6174.
- 32 (52) Ando, T.; Izhar, S.; Tominaga, H.; Nagai, M. Ammonia-Treated Carbon-Supported  
33 Cobalt Tungsten as Fuel Cell Cathode Catalyst. *Electrochim. Acta* **2010**, *55*,  
34 2614–2621.
- 35 (53) Tang, H.; Tian, X.; Luo, J.; Zeng, J.; Li, Y. A Co-Doped Porous Niobium Nitride  
36 Nanogrid as an Effective Oxygen Reduction Catalyst. *J. Mater. Chem. A* **2017**, *5*,  
37 14278–14285.
- 38 (54) Liu, Y.; Jiang, H.; Zhu, Y.; Yang, X.; Li, C. Transition Metals (Fe, Co, and Ni)  
39 Encapsulated in Nitrogen-Doped Carbon Nanotubes as Bi-Functional Catalysts  
40 for Oxygen Electrode Reactions. *J. Mater. Chem. A* **2016**, *4* (5), 1694–1701.

- 1 (55) Chen, T.; Guo, S.; Yang, J.; Xu, Y.; Sun, J.; Wei, D.; Chen, Z.; Zhao, B.; Ding, W.  
2 Nitrogen-Doped Carbon Activated in Situ by Embedded Nickel through the Mott-  
3 Schottky Effect for the Oxygen Reduction Reaction. *ChemPhysChem* **2017**, *18*  
4 (23), 3454–3461.
- 5 (56) Shinagawa, T.; Garcia-Esparza, A. T.; Takane, K. Insight on Tafel Slopes from  
6 a Microkinetic Analysis of Aqueous Electrocatalysis for Energy Conversion. *Sci.*  
7 *Rep.* **2015**, *5*, 13801–13821.
- 8 (57) Yan, B.; Krishnamurthy, D.; Hendon, C. H.; Yan, B.; Krishnamurthy, D.; Hendon,  
9 C. H.; Deshpande, S. Surface Restructuring of Nickel Sulfide Generates Optimally  
10 Coordinated Active Sites for Oxygen Reduction Catalysis Surface Restructuring of  
11 Nickel Sulfide Generates Optimally Coordinated Active Sites for Oxygen  
12 Reduction Catalysis. *Joule* **2017**, *1*, 600–612.
- 13 (58) Soo Kang, J.; Park, M. A.; Kim, J. Y.; Ha Park, S.; Young Chung, D.; Yu, S. H.;  
14 Kim, J.; Park, J.; Choi, J. W.; Jae Lee, K.; Jeong, J.; Jae Ko, M.; Ahn, K-S.; Sung,  
15 Y-E. Reactively Sputtered Nickel Nitride as Electrocatalytic Counter Electrode for  
16 Dye- and Quantum Dot-Sensitized Solar Cells. *Sci. Rep.* **2015**, *5*, 10450–10460.
- 17 (59) Biesinger, M. C.; Payne, B. P.; Lau, L. W. M.; Gerson, A.; Smart, R. S. C. X-Ray  
18 Photoelectron Spectroscopic Chemical State Quantification of Mixed Nickel Metal,  
19 Oxide and Hydroxide Systems. *Surf. Interface Anal.* **2009**, *41* (4), 324–332.
- 20 (60) Weidler, N.; Schuch, J.; Knaus, F.; Stenner, P.; Hoch, S.; Maljusch, A.; Schäfer,  
21 R.; Kaiser, B.; Jaegermann, W. X-Ray Photoelectron Spectroscopic Investigation  
22 of Plasma- Enhanced Chemical Vapor Deposited NiOx, NiOx(OH)y, and  
23 CoNiOx(OH)y: Influence of the Chemical Composition on the Catalytic Activity for  
24 the Oxygen Evolution Reaction. *J. Phys. Chem. C* **2017**, *121*, 6455–6463.
- 25 (61) Grosvenor, A. P.; Biesinger, M. C.; Smart, R. S. C.; McIntyre, N. S. New  
26 Interpretations of XPS Spectra of Nickel Metal and Oxides. *Surf. Sci.* **2006**, *600*  
27 (9), 1771–1779.
- 28 (62) Leineweber, A.; Jacobs, H.; Hull, S. Ordering of Nitrogen in Nickel Nitride Ni<sub>3</sub>N  
29 Determined by Neutron Diffraction. *Inorg. Chem.* **2001**, *40* (23), 5818–5822.
- 30 (63) Nagakura, S.; Ōtsuka, N.; Hirotsu, Y. Electron State of Ni<sub>4</sub>N Studied by Electron  
31 Diffraction. *J. Phys. Soc. Japan* **1973**, *35* (5), 1492–1495.
- 32 (64) Abroshan, H.; Bothra, P.; Back, S.; Kulkarni, A. R.; Norskov, J. K.; Siahrostami, S.  
33 An Ultra-Thin Cobalt-Oxide Overlayer Promotes Catalytic Activity of Cobalt Nitride  
34 for Oxygen Reduction Reaction. *J. Phys. Chem. C* **2018**, *122* (9), 4783–4791.
- 35 (65) Seh, Z. W.; Kibsgaard, J.; Dickens, C. F.; Chorkendorff, I.; Nørskov, J. K.;  
36 Jaramillo, T. F. Combining Theory and Experiment in Electrocatalysis: Insights  
37 into Materials Design. *Science* **2017**, *355* (6321).

38

39

1 TOC image:



2

3